PCCP

Accepted Manuscript

ROYAL SOCIETY OF CHEMISTRY

www.rsc.org/pccp

Unraveling the Ultrafast Behavior of Nile Red Interacting with an Aluminum and Titanium Co-doped MCM41 Materials†

Cristina Martin, [1] Boiko Cohen, [1] María Teresa Navarro, [2] Avelino Corma,[2] and Abderrazzak Douhal*,[1]

[1] *Departamento de Química Física, Facultad de Ciencias Ambientales y Bioquímica, and Inamol, Universidad de Castilla-La Mancha, Avda. Carlos III, S.N., 45071 Toledo, Spain.*

[2] *Instituto de Tecnología Química, UPV-CSIC, Avenida de los Naranjos s/n, 46022 Valencia, Spain.*

* corresponding author: Abderrazzak Douhal, email: abderrazzak.douhal@uclm.es, Phone number: +34-925-265717

† Electronic Supplementary Information (ESI) available: Table S1 lists the structural properties and metal contents of the final X-Y-MCM41. Figures S1, S2 and Table S2 show the spectral deconvolution, as well as the values obtained of absorption of NR interacting with X-YMCM41 at different Si/X and Si/Y atomic ratio. Figures S3-S5: Femtosecond-emission transients for NR/X-MCM41(X= Ti, Al and Ti/Al) at different doping metal upon excitation 562 nm and at several observation wavelengths. See DOI:

Abstract

We report on the spectroscopic and photodynamical characterizations of Brønsted and Lewis acid sites within solids on the behaviors of Nile Red (NR) upon interaction with single- and multi-metal(X)-doped MCM41 materials (X= Ti and/or Al) in dichloromethane (DCM) suspensions. The steady-state results show that the H-bonding ability of doped MCM41-based materials leads to different NR populations (monomers, H- and J-aggregates), where their contribution are related to the type of site acidity (Brønsted or Lewis) and percent of acid sites (Si/X atomic ratio) in the silica framework. While at different Al doping contents the interacting NR populations suffer slight modifications, an increment on the Ti content induces a substantial increase in the J-aggregate formation. Moreover, the picosecond time-resolved data not only confirm the H-bonding interaction between the X-MCM41 hosts and the different types of NR populations, but also indicate that the S_1 deactivation pathways of these populations are connected to the Brønsted and Lewis acidities of the host. The shortening in the emission lifetimes of NR species is significantly associated with increased Lewis acidities (Ti doping). The femtosecond dynamics of loaded NR in single and multiple metal doped MCM41 show that the charge separation (CS) state (formed in ~ 200 – 370 fs) and the subsequent electron injection (EI) process (~ 200 fs) are sensitive to the content and type of acid sites. These observations are based on the time shortening of the CS formation from ~350 fs in the NR/Al-MCM41 samples (at 1% of Al) to < 200 fs in the NR/Ti-MCM41 composites. For NR/Ti-Al-MCM41 sample, the observed change is directly related to the Ti content: at 1% of Ti, the CS is formed in ~ 300, while at 3% of Ti it becomes < 200 fs. The same behavior is observed for the EI event, where the probability of having it, is related to the Ti presence and content: higher doping contents result in a faster EI process (from ~ 250 fs to ~150 fs). Therefore, the interactions of these co-metal-doped MCM41 materials (the Ti-Al-MCM41 ones) with NR show a competition between the Brønsted (Al doping) and Lewis (Ti doping) acid sites. Our findings may help in a better understanding of the reactivity within metal-doped mesoporous catalysts and could be used in related fields like drug delivery and nanophotonics using-silica materials.

1. Introduction

Zeolites and mesoporous materials are widely used as catalysts in petrochemical processes, pharmaceutical procedures or environmental pollution control.[1-5] However, the pore size restriction of zeolites (only few nanometers), hinders the encapsulation of large reactant molecules and consequently reduces their applicability. To solve this problem, the use of mesoporous materials, in particular MCM41, which presents a tunable pore size as well as simplicity of the synthetic methodologies, easy modification and functionalization,[2, 4, 6] offers one of the best alternatives.

Nowadays, the tendency on the doping of MCM41 with single-acid-sites in the framework is moving to the preparation of multi-acid-sites solids (by a simultaneous introduction of Brønsted and Lewis sites).[7, 8] Considerable efforts have been made aiming to reach a sequential catalytic process using only one-pot operation, which will reduce the number of synthetic steps and the related purification process.[9, 10] However, to get an ideal multifunctional catalyst for one-pot multistep reactions could be difficult due to the large number of chemical and physical events to control, such as the interactions arising between the different sites and species involved in the reaction as well as the necessity to achieve an operation window.[7, 9] This complexity has been observed, for instance, in the oxidation of cyclic olefins, like Ti-Al-Beta zeolites, which presents higher conversion per Ti ratios than the Ti silicalite (TS-1) for bulkier reactants.[7-11] However, in epoxide formation, the presence of Al (Brønsted sites) in Ti-Al-Beta zeolites induces a lower selectivity of the formed product.[7-11] The multi-sites solid catalysts provide different possibilities than the separate single-sites in homogeneous and heterogeneous processes, as a result of a change in the physicochemical properties of such material. Those changes could affect the molecule-matrix interactions reflected in the reaction outcome and mechanism.[7-11]

Therefore, the knowledge of the interplay and cooperation between the two catalytic metal active sites through detailed information on the specific and non-specific interactions between organics and silica-based materials would help in understanding the key factors that govern the reactions involved in multi-sites hybrid-materials. Experimental and computational studies have been made in this direction; [4, 7, 9, 11, 12] however, an accurate characterization of the surface properties is still required. From this point of view, powerful analytical tools that enable obtaining precise information on the catalysts would facilitate a comprehension of the reaction pathways, an improvement in the selectivity of the product formation, and a better understanding of their dependence with the experimental conditions. Among the vast arsenal

of techniques, the use of time-resolved spectroscopic tools with dyes sensitive to the microenvironment, [13-16] would give important information on the reaction pathways at the very first occurring events (on femto- and picosecond time regimes).[13, 14, 17]

One of the best aromatic dyes to explore how the MCM41 framework composition affects the acidity of the materials is Nile Red (NR). [18-23] This dye undergoes intramolecular charge transfer (ICT) process at the S_1 state, thus being sensitive to the nature of the environment (polarity and H-bonding ability), leading to rich spectroscopic and dynamical behaviors.[18-22] Recently, the applicability of this dye in the acidity characterization of different metal doped MCM41 materials (X-MCM41, X = Al, Ga, Ti, Zr) has been successfully demonstrated, and it has been found that the spectral and dynamical properties of the NR depend on the type of the doping metal.[23] However, to the best of our knowledge, the influence of different amounts of Ti and Al atoms in the MCM41 framework, as well as the simultaneous presence of Ti and Al co-doping the MCM41 (Ti-Al-MCM41) material using NR as a local sensor have not yet been studied at high temporal resolution. Furthermore, tough site concentration and the presence of multiple reaction sites are important catalytic variables.

Herein, we report on the photophysical behavior of NR interacting with X-MCM41, Y-MCM41, and X-Y-MCM41 hybrids by probing the involved interactions within the formed complexes (with and without different Si / X or Y doping metals, where X is Ti and Y is Al) in dichloromethane (DCM) suspensions. The results show, as observed in single-site doped MCM41, that upon interaction with Ti-Al-MCM41 at different Si/Ti ratios, the different Brønsted/Lewis acidities lead to the formation of different NR populations (monomers, J- and H-aggregates). However the contribution of each population in the Ti-Al-MCM41 material is defined by the Si/Ti ratio in the framework. On the other hand, the femtosecond experiments reveal that simultaneous presence of Ti and Al sites on the MCM41 matrix affects the early dynamics of NR in comparison to the single-doped Ti-MCM41 or Al-MCM41 using the same Si / metal ratios. We found that for NR/Ti-Al-MCM41-(1%,1%) composites (at 1% of both Ti and Al atoms), the formation of a charge separation (CS) state in excited NR occurs in ~ 300 fs, while the electron injection (EI) process to the trap states is not detected for Ti-MCM41-(1%) (at 1% of Ti). On the contrary, for NR/Ti-Al-MCM41-(3%,1%) composites (at 3% of Ti and 1% of Al atoms) the CS state formation happens in < 200 fs and the EI to the trap states occurs in ~210 fs. However, the time constants for the EI processes are longer than the observed ones for NR/Ti-MCM41-(3%). These results can be explained in terms of the

different interactions of NR with Ti-Al-MCM41, resulting from the variation in the Lewis strengths due to different Ti coordination in the MCM41 containing Al atoms.

These findings might be useful in the design of multi-sites catalytic materials and open the door for other applications such as developing polarity and acidity/basicity sensors of silica-based materials, nanophotonics or drug-delivery systems.

2. Experimental part

Nile Red (NR) and dichloromethane (DCM, spectroscopic grade > 99.5%) were purchased from Sigma-Aldrich and used without further purification. The samples with MCM41 containing titanium and/or Aluminium were prepared using amorphous silica (Aerosil200, Degussa), hexadecyltrimethylammonium bromide (C_{16}TMABr 98%wt, Sigma-Aldrich), and tetramethylammonium hydroxide (25% wt TMAOH in water, Sigma-Aldrich). The sources of titanium and aluminium are titanium tetraethoxide (99%, Sigma-Aldrich), and aluminium oxide (99.9%, Sigma-Aldrich), respectively. Details about the synthesis and characterization procedures of the X-Y-MCM41 hosts, as well as the table of the structural properties and metal contents (Table 1S), are given in the Supporting Information.

Steady-state UV-visible absorption and diffuse transmittance spectra were recorded on Jasco V-670 equipped with a 60 mm integrating sphere ISN-723. Emission spectra were recorded using Fluoromax-4 (Jobin-Yvone). The emission lifetimes were measured using a picosecond (ps) time-correlated single-photon-counting (TCSPC) spectrophotometer (FluoTime 200, PicoQuant) described elsewhere.[24] The samples was excited by a 40 ps-pulsed (< 1 mW, 40 MHz repetition rate) diode-laser (PicoQuant) centered at 635 nm (instrument response function, IRF ~ 80 ps). The fluorescence signal, gated at magic angle (54.7°), was monitored at a 90° angle to the excitation beam at discrete emission wavelengths. Decay data was analyzed using the FluoFit software package (PicoQuant). Exponential decay functions were convoluted with the experimental IRF and fit to the experimental decay. The quality of the fits, as well as the number of exponentials, were carefully selected based on the reduced χ^2 values (which were ≤ 1.1) and the distributions of the residuals.

The femtosecond emission transients have been collected using the fluorescence up-conversion technique.[25] The system consists of a femtosecond optical parameter oscillator (Inspire Auto 100) pumped by 820 nm pulses (90 fs, 2.5 W, 80 MHz) from a Ti:sapphire oscillator MaiTai HP (Spectra Physics) to generate the different excitation beams at 562, 600, 616 nm (~0.1 nJ). The polarization of the latter was set to magic angle with respect to the fundamental beam. The sample has been placed in a 1-mm thick rotating cell. The

fluorescence was focused with reflective optics into a 0.3 mm BBO crystal and gated with the fundamental femtosecond beam. The IRF of the apparatus (measured as a Raman signal of pure solvent) was ~200 fs (full width at half maximum, fwhm) for all the excitation wavelengths. To analyze the decays, a multiexponential function convoluted with the IRF was used to fit the experimental transients. In all the cases, the errors for the calculated time constants were smaller than 15%. All the experiments were performed at room temperature (293 K).

3. Results and Discussion

3.1. Steady-state UV-visible Absorption and Emission Studies in DCM suspensions

3.1.1. NR interacting with Al-MCM41 at different Si/Al doping ratios

Introducing trivalent metals (X) in MCM41 framework induces different acid-base properties of the material.[4, 26-28] These are further affected by the Si / X ratio.[29, 30] We first present the effect of different Si/Al ratios in MCM41 on the interactions between NR and the silica surface, as well as on the variation of the dye populations. Figure 1A shows the normalized diffuse transmittance (DT) spectra of DCM suspensions containing NR interacting with R-MCM41 and with MCM41 doped with isomorphic Al (Al-MCM41) at different Si/Al doping ratio (1% and 3%). The DT spectra are composed by four bands (Figure S1, ESI) centered at ~ 557, 590, 617 and 645 nm, assigned to dye molecules weakly interacting with the host, H-aggregates, monomers, and J-aggregates, respectively, in agreement with our previous report.[23] Although the maximum absorption wavelengths for each component of the three samples (R-MCM41, Al-MCM41-(1%) and Al-MCM41-(3%)) are similar, the relative contributions to the total spectrum intensities are different. These variations reflect a change in the chemical framework composition, where the substitution of 1% or 3% of the Si atoms by Al ones modifies the interactions between the host and NR as a result of formation of new Brønsted sites in MCM41.[4, 26, 28] Therefore, when the replacement of Si with Al atoms is larger, an increment in the electronic charge defects in the host framework is produced, and consequently its Brønsted framework acidity increases. [29, 30] At higher Al doping, the host-guest interactions become stronger, and as a consequence the population of weakly interacting NR species is reduced, while the J- and H-aggregate populations show an opposite tendency. This behavior is in agreement with the results obtained for regular mesoporous material (R-MCM41) and for Al-MCM41-(3%), where the generation of more Brønsted sites results in a preferential formation of J- and H-aggregates in comparison with the remaining populations.[23]

Figure 2A shows the stationary emission spectra of NR/R-MCM41, NR/Al-MCM41-(1%) and NR/Al-MCM41-(3%) upon excitation at 600 nm. The broad emission spectra result from the combined emission of different populations: NR monomers (~ 670 nm) and J-type aggregates (~ 720 nm), while the emission of the H-type aggregates is inhibited due to the forbidden excitonic transitions (very weak to be detected in a stationary detection mode).[31-33] The observed results are in agreement with those previously published for the NR/Al-MCM41-(3%) hybrids, where the observed differences between R-MCM41 and Al-MCM41 at different Al contents can be explained in terms of the increase in the host acidity.[23]

3.1.2. NR interacting with Ti-MCM41 at different Si/Ti doping ratios

Here, we report how the Si/Ti ratio in the doped MCM41 influences the NR-matrix interactions. The Si substitution with Ti atoms does not alter the electroneutrality of the MCM41 framework. However new Lewis acid sites are generated due to the presence of free d-orbitals in Ti atoms. [4, 26, 27, 34] Figure 1B shows, the DT spectra of NR interacting with Ti-MCM41 at different Si/Ti doping ratio (1%, 3% and 5%), in addition to the DT spectra using R-MCM41 host. The spectra are composed by different populations absorbing at ~ 585, 615 and 661 nm, assigned to H-type aggregates, monomers and J-type aggregates, respectively, in similarity with the NR/Al-MCM41 complexes (Figure S1, ESI). The absorption band of NR molecules weakly interacting with the host (normally at ~555 nm) is not present even at low Ti doping. This is in agreement with the previous report on NR/Ti-MCM41-(1%) in DCM suspension.[23] On the other hand, the J-type aggregates population is more favored at higher Ti doping ratio. These observations could be explained in terms of an increment in the Lewis acidity sites due to the increase in the Ti doping,[35, 36] and therefore an enhancement in the host-guest interactions strength.

Figure 2B shows a comparison between the emission spectra of NR/R-MCM41, NR/Ti-MCM41-(1%), NR/Ti-MCM41-(3%) and NR/Ti-MCM41-(5%) in DCM suspensions upon excitation at 600 nm. For NR/Ti-MCM41 composites, the spectra reflect the contribution of the emission from NR monomers (~ 670 nm) and J-type aggregates (~ 720 nm), as they are observed for NR/Al-MCM41 complexes when varying Si/Al doping ratio. However, in the case of NR/Ti-MCM41 in DCM suspension, there is a clear effect of the Si/Ti doping ratio on the maximum spectral position, where a higher Ti doping ratio induces a larger stokes shift (from ~ 210 to 470 cm^{-1}). These spectral shifts are a result of an increment in the Lewis acidity of the framework at higher Ti doping ratio,[35, 36] which stabilizes the intramolecular charge transfer (ICT) excited state of NR.[23]

3.1.3. NR interacting with Ti-Al-MCM41 at different Si/Ti and Si/Al doping ratios

The chemical structure of the MCM41 framework allows simultaneous functionalization with Brønsted and Lewis acid sites on a single support. This multifunctional solid catalyst is obtained by simultaneous isomorphic substitution of the Si atoms with Al (Brønsted sites) and Ti (Lewis sites) atoms.[7, 8] The host-guest interactions using this kind of MCM41 material will be directly related to the overall acidity of the framework. [7, 8] Thus, we studied the composites of NR with MCM41 co-doped with Al and Ti atoms. Figure 1C shows the DT spectra of Ti-Al-MCM41 at different Si/Ti doping ratio (1%, 3%) with the Si/Al ratio kept constant (1%), in addition to those using Al-free Ti-MCM41-(1%) and Ti-free Al-MCM41-(1%) materials. Table S2 and Figure S2, (panels A and B), ESI, exhibit the results of the deconvoluted DT spectra of NR/Ti-Al-MCM41-(1%, 1%) and NR/Ti-Al-MCM41-(3%,1%). The spectra are composed by five bands centered at ~ 559, 588, 615, 643 and 665 nm. In similarity with the single metal-atom doped MCM41 composites, the first component (~ 559 nm) is assigned to NR weakly interacting with the host surface. The 588 and 615 nm components are similar to the H-aggregates and monomers ones observed in the NR/Al-MCM41 (~ 593 and 615 nm) and in the NR/Ti-MCM41 (~ 585 and 615 nm), and therefore are respectively assigned to those species. On the other hand, the presence of the 643 nm component, which was observed in the NR/Al-MCM41 samples but not for the NR/Ti-MCM41 ones, indicates the presence of J-type aggregates formation in the vicinity of Al centers. In the same way, the ~ 665 nm component is only present in the NR/Ti-MCM41 samples, which suggests that J-type aggregates are also formed in a comparable environment to that of Ti. It is worth noting that, although the relative contributions of J-aggregates absorption to the total DT spectrum intensity in NR/Ti-Al-MCM41–(1%, 3%) are slightly different (only a small increment of the J-aggregate contribution in Ti vicinity was observed), they differ from those observed for NR/Ti-MCM41-(1%, 3%) sample. Therefore, the presence of Al atoms in the MCM41 framework modifies the NR nature populations within the Ti-Al-MCM41, leading to species similar to those of the NR/Al-MCM41 samples. These changes can be explained by the electronegativity modification of the MCM41 framework, as observed for Ti-Beta Zeolites,[37] which favored Brønsted interactions between the host and NR molecules. In addition to this effect, the Ti coordination in MCM41 (as in zeolites) can be modified by the influence of Al which affects the stability of the Ti LUMO, and consequently the Lewis strength.[11, 37, 38] Both effects alter the Brønsted/Lewis interactions between NR molecules and MCM41 host, and result in a behavior more reminiscent to the NR/Al-MCM41 systems than to the Ti-MCM41 ones, even when the doping of the Ti in the Ti-Al-MCM41

material is higher. In other words, NR adsorption sites associated with the presence of Al in the framework predominate those related to Ti, when NR is used as a probe molecule for metal doped MCM41.

Figure 2C shows the emission spectra (λ_{exc}= 600 nm) of NR/Ti-Al-MCM41-(1%,1%) and NR/Ti-Al-MCM41-(3%,1%) in comparison with the Ti-MCM41-(1%) and Al-MCM41-(1%) ones. The NR/Ti-Al-MCM41 spectra of both samples are overlapped with the NR/Al-MCM41 one and thus, the blue part of the spectra corresponds to the emission of the monomers, while the red shoulder is assigned to the one of the J-type aggregates. These results point out that the Brønsted acidity interactions are more favored than the Lewis acidity ones, as it is also suggested by the behavior of the DT spectra.

3.2. Picosecond Time-Resolved Measurements

To get information on the fluorescence lifetimes of NR interacting with the described doped MCM41 mesoporous materials in DCM suspensions, picosecond (ps) time-correlated single photon counting (TCSPC) measurements were performed upon excitation at 635 nm. Figure 3 shows the emission decays of the studied samples collected at 670 nm, and Tables 1 and 2 give the values of the time constants and their relative pre-exponential factors obtained from a multiexponential fit of the experimental data.

3.2.1. NR interacting with Al-MCM41 at different Al doping ratios

Figure 3A and Table 1 show that the behavior of the emission decays of the NR/Al-MCM41 samples at different Al doping (1% and 3%) in DCM suspensions are multiexponential. The observed lifetimes and relative amplitudes for the NR/Al-MCM41-(1%) decays (τ_1 ~ 0.34 ns (30 - 21 %), τ_2 ~ 1.28 ns (59 - 63 %) and τ_3 ~ 2.7 ns (18 - 12 %)) are comparable to those obtained for the NR/Al-MCM41-(3%) samples, and are assigned to H-aggregates, J-aggregates and monomers, respectively.[23] Thus, only a weak effect of the Al content on the picosecond decay of NR/Al-MCM41 composites is observed. Although the presence and increase of Al doping in the MCM41 matrix leads to formation of Brønsted acid sites, [29, 30] the lack of significant change in the emission decays using Al-MCM41 with a 1% or 3% of Al content can be explained by a delocalization of the produced charge in the silica MCM41 framework which reduces the effect of the increased Brønsted acid sites in the material.

3.2.2. NR interacting with Ti-MCM41 at different Ti doping ratios

In contrast to the case of NR/Al-MCM41 at different Si/Al ratios, the fluorescence lifetimes of NR molecules using Ti doping, as well as the values of the relative contributions of the components, show a strong dependence on the Si/Ti ratio (Table 1 and Figure 3C). The fluorescence lifetimes of the NR/Ti-MCM41-(3%) components are τ_1 = 0.09 ns (60 – 65 %); τ_2 = 0.55 ns (26 – 27 %) and τ_3 = 1.82 ns (14 – 8 %), while for the NR/Ti-MCM41-(5%) one they are τ_1 = 0.07 ns (66 – 69 %); τ_2 = 0.40 ns (23 – 24 %) and τ_3 = 1.47 ns (11 – 6 %). In a previous report, the results of NR/Ti-MCM41-(1%) showed a notable quenching of the fluorescence lifetimes of the monomers H-and J-aggregates,[23] in comparison to the NR/R-MCM41 sample (Figure 3B and Table 1). Moreover, we have observed that for the NR/Ti-MCM41-(1%) in DCM suspensions the fluorescence lifetimes of the monomers, H- and J-aggregates are τ_1 ~ 0.16 ns, τ_2 ~ 0.74 ns and τ_3 ~ 1.96 ns, respectively. [23] The lifetimes shortening could be explained by electron injection (EI) into the trap states formed by the d-orbitals of the Ti atoms presented in the MCM41 matrix.[39, 40] Thus, the decrease in the emission lifetimes when increasing the Ti content, as well as the changes in the relative contributions at different Si/Ti atomic ratios, reflect that the EI process in these hybrid materials is strongly affected by the presence of Ti on the framework. Although the variation in the value of the shorter components is within the experimental error (10 -15 %), its relative contribution is increasing with the Ti content in the MCM41 framework, from ~ 49 % in Ti-MCM41-(1%) to ~ 69 % in Ti-MCM41-(5%) (the ultrafast nature of the EI, which occurs below the resolution of the ps-spectrometer, can affect the real contribution of the τ_1 component in the emission decays of the NR/Ti-MCM41 samples (Ti = 1%, 3% and 5%)). Hence, the EI from monomers, as well as from the H- and J-aggregates of NR to the Ti-MCM41 is favored at higher Ti doping as a result of an increment in the number of Ti atoms, [35, 36] which in turn produces more trap states in the MCM41 framework. On the other hand, this change is more pronounced when the Ti content changes from 1% to 3% in the MCM41 lattice than when it increases from 3% to 5%. Since MCM41 is amorphous, the Ti atoms are not in equivalent positions within the MCM41 framework, and as a result the Ti coordination number and local geometry can vary, leading to a different stabilization of the trap states,[11] thus modifying the Lewis acidity strength of the whole framework. Another process that can further affect the Lewis acidity strength at higher Ti doping (> 3%) is the possibility of formation of Ti-O-Ti chemical bonds. [41, 42] Such Ti cluster formation can modify the position of LUMO of the trap states and thus influence the efficiency and the dynamics of the EI process. [11, 37, 38] Additionally, it has been reported that, at larger Ti contents, the probability of having some of the Ti atoms less accessible for the guest in the MCM41 increases.[41] Finally,

we consider the possibility that the observed decrease in the emission lifetimes is due to changes in the confinement because of the increased Ti content in the MCM41 framework. Although we cannot entirely discard the confinement effect, the negligible effect that the Al doping has on the emission decays of NR indicates that in the NR/Ti-MCM41 complexes the observed decrease in the obtained lifetime values are mostly related to the EI into the trap states processes. In a previous work, we reported that the emission lifetime of NR changes from a monoexponential in DCM solution (τ = 4.4 ns) to a multiexponential behavior (τ_1 = 0.32 ns, τ_2 = 0.92 ns and τ_3 = 2.5 ns) when interacting with R-MCM41.[23] These results were explained in terms of formation of H- and J-aggregates in the confined space of the host, as well as the contribution of NR monomers attached to the MCM41 surface. Furthermore, it was demonstrated that the presence of tri-valent metal atoms (Al or Ga) in the host matrix only slightly affects the fluorescence lifetime values of the NR species in comparison with the NR/R-MCM41complexes.[23] This observation indicates that the presence of tri-valent metals in the host framework does not affect significantly the NR photodynamics. In agreement with the present results, when the doping metal was tetravalent (Ti or Zr), the observed lifetimes became lower in comparison with the R-MCM41.[23] Similarly, this effect was assigned to an EI into the trap states (femtosecond time scale) formed efficiently by the d-orbitals of the Ti or Zr atoms in the MCM41 lattice.

3.2.3. NR interacting with Ti-Al-MCM41 at different Ti doping ratios

A simultaneous isomorphic substitution of the Si atoms with Al (Brønsted sites) and Ti (Lewis sites) on the MCM41 framework is expected to change the specific and non-specific interactions of the NR with the mesoporous host. Thus, to analyze the effect of these changes on the fluorescence lifetimes of NR populations, we compare the values obtained for NR/Ti-Al-MCM41-(1%,1%) and NR/Ti-Al-MCM41-(3%,1%) with those observed for NR/Al-MCM41-(1%) and NR/Ti-MCM41-(1%) (Figure 3C and Tables 1 and 2). The emission lifetimes of the monomers, H- and J-aggregates in NR/Ti-Al-MCM41-(1%,1%) and NR/Ti-Al-MCM41-(3%,1%) (τ_1 = 0.09 ns, τ_2 = 0.55 ns and τ_3 = 1.82 ns) are shorter than to the ones observed for the NR/Al-MCM41 sample (τ_1 ~ 0.34 ns, τ_2 ~ 1.28 ns and τ_3 ~ 2.7 ns). This result shows that the presence of Ti atoms embedded in the Al-MCM41 matrix induces faster dynamics as a consequence of an EI process. On the other hand, the fluorescence lifetimes of the NR/Ti-Al-MCM41-(1%,1%) and NR/Ti-Al-MCM41-(3%,1%) complexes are longer than those observed for NR interacting with Ti-MCM41, even for lower Ti doping ratios in the latter, we got τ_1 ~ 0.16 ns, τ_2 ~ 0.74 ns and τ_3 ~ 1.96 ns. These results, along with the smaller relative contribution of the shortest component, suggest that in the Ti-Al-MCM41 samples,

the EI is disfavored. This reflects a delocalized Brønsted acidity in the framework as a result of the Al presence on the lattice. As explained earlier, the introduction of Al atoms in the framework modifies the overall electronegativity of the framework and the Ti sites disposition in the MCM41,[11, 37, 38] leading to an increment in the Brønsted interactions between the NR and the framework, in detriment of the Lewis ones.

3.3. Femtosecond Emission Measurements

To obtain detailed information on the early dynamics of NR interacting with the studied X-MCM41 materials in DCM suspensions, we recorded femtosecond (fs) emission transients at different observation wavelengths following excitation at 562 nm. Figures 4, 5 and 6, as well Figures 3S, 4S and 5S, show the obtained decays of the studied samples. Tables 3A and B give the time constants and pre-exponential factors using a multi-exponential fit convoluted with an IRF of 200 fs.

3.3.1. NR interacting with Al-MCM41 at different Si/Al doping ratios

We begin with the results obtained for NR interacting with Al-MCM41-(1%) and Al-MCM41-(3%) in DCM suspensions (Figures 4 and S3, ESI and Table 3A). At the shortest gated wavelengths of the spectra (630-650 nm), the signals decay multiexponentially with time constants of τ_1 ~ 0.37 ps, τ_2 ~ 3.3 ps and τ_3 ~ 0.3 ns (fixed in the fit using the value obtained from the ps-emission decays), at the longest ones (670-700 nm), the fits show a fs-rising component with a time constant of ~ 0.30 ps and a offset (~ 0.3 ns). The femtosecond dynamics of NR in solution are characterized by a charge separation (CS) state after an intramolecular charge-transfer (ICT) process from the diethylamino group to the carbonyl side, which in DCM occurs in ~ 1 ps. [25-26, 23, 43] Furthermore, the time constant of the ICT reaction is affected by the properties of the environment (polarity and H-bond)[44, 45] due to variation in the energy barrier between the locally excited (LE) and the CS states.[20, 21, 43] Moreover, we have previously demonstrated that the ICT process in NR is also dependent on the silica framework composition, where the used metal doping atoms would stabilize the CS state in different ways.[23] Based on these observations the sub-fs component is assigned to the formation of the CS state of NR interacting with the A-MCM41 host. The 3 – 4 ps decaying component is due to vibrational cooling (VC) at S_1 of the CS state. Within our time resolution (IRF ~ 200 fs), the ultrafast study shows that the CS state formation is not significantly affected by the increment of the Al doping (from 1% to 3%) in the host framework.

3.3.2 NR interacting with Ti-MCM41 at different Si/Ti doping ratios

To examine the influence of the Lewis acidity of the MCM41 on the ultrafast dynamics of NR interacting with the mesoporous hosts, the fs-emission transients using Ti-MCM41-(1%), Ti-MCM41-(3%) and Ti-MCM41-(5%) materials in DCM suspensions were recorded. Figures 5 and S4, ESI show the emission transients observed at representative observation wavelengths, and Table 3 lists the time and amplitude values obtained from the multiexponential fits. For the three studied samples, the longest time constant (τ_3 =0.16 ns, 0.09 ns and 0.07 ns, respectively) were fixed in the fits and used from the ps-emission studies. In addition to τ_3 component, the fits at the 630-670 nm region give time constants of $\tau_1 \sim 0.22$, 0.17 and 0.14 ps, and $\tau_2 \sim 2.2$, 1.8 and 1.7 ps for Ti-MCM41-(1%), Ti-MCM41-(3%) and Ti-MCM41-(5%), respectively. On the other hand, at the reddest part of the spectra the absence of a rising component indicates that τ_1 decaying component is due to the EI process, which is in agreement with the previous study of NR/Ti-MCM41-(1%) complexes.[23] Thus the ultrafast short components (τ_1) is assigned to the EI process from the photoproduced CS state of NR to the Ti trap states, while τ_2 is due to the VC of the CS state. The ICT reaction time should be lower than our time resolution (IRF ~ 200 fs).

Although the origin of the dynamical behaviour is the same, there is a decrease in the value of the time components upon increasing the Ti loading in the MCM41 framework (Figure 5, Table 3). This effect can be explained by an increase in the population of Lewis trap states formed by the d-orbitals of Ti atoms. [35, 36] Thus, in Ti-MCM41-(5%) the EI process is more probable than in Ti-MCM41-(3%) and in Ti-MCM41-(1%), leading to a shortening of the global dynamics. Furthermore, the decrease of the relative amplitudes of the offset (τ_3) in NR/Ti-MCM41-(5%) (45 %) in comparison to the one observed in NR/Ti-MCM41-(1%) (75%) reflects the presence of a non-radiative channel like that of EI process leads to a decrease in the population of emitting states. It is worth to note, as observed also in the ps-emission studies, that the effect of the Ti in the MCM41 lattice is more pronounced when the Ti doping goes from 1% to 3%, while at a higher Ti content, the probability of having part of the Ti atoms inaccessible, and thus unable to interact with the NR, increases. [41] Additionally, at higher Ti doping one needs to take into account the possibility of Ti-O-Ti formation,[41, 42] which in turn can also affect the EI process by modifying the energy of the LUMO of the trap states. [11, 37, 38]

3.3.3. NR interacting with Ti-Al-MCM41 at different Si/Ti doping ratios

Now, we focus on the influence of simultaneous substitutions of Si with Al and Ti atoms in the MCM41 lattice on the ultrafast dynamics of NR. The fs-emission transients of NR/Ti-Al-MCM41-(1%,3%) and NR/Ti-Al-MCM41-(3%,1%) were recorded upon excitation

of in DCM suspensions at 560 nm. Figures 6 and S5, ESI, and Table 3 show the obtained emission transients and the parameters from multiexponential fits of the experimental data. The fits at 630 – 650 nm region give time constants of τ_1 ~ 0.30 and 0.20 ps, and τ_2 ~ 2.5 and 1.88 ps, for NR/Ti-Al-MCM41-(1%,1%) and NR/Ti-Al-MCM41-(3%,1%)%, respectively. At longer observation wavelengths (670 – 700 nm) the NR/Ti-Al-MCM41-(1%,1%) decay fits give a rising component (τ_1) while for the NR/Ti-Al-MCM41-(3%,1%) the τ_1 component is not needed. Additionally, we found a long time constants (0.30 ns and 0.20 ns) observed at the whole spectra, and which were fixed in the fit using the values obtained from the ps-emission decays. The comparison of these results with those of the two single doped MCM41 materials (NR/Al-MCM41-(1%) and NR/Ti-MCM41-(1%)) shows that when the Ti doping in the Al-MCM41 framework is small, the resulting ultrafast dynamics is similar to that observed for the Al-MCM41samples (without Ti). Thus, the τ_1 component in the co-doped complexes with 1% of Ti and 1% of Al corresponds predominantly to ICT reaction time and τ_2 arises from the VC of the CS forms at the S_1 state (Scheme 1). On the other hand, the values of these time constants are shorter than those observed in Al-MCM41-(1%) (τ_1 is reduced from 360 fs to 290 fs while for τ_2 it goes from 3.20 ps to 2.90 ps), which reflects the presence of Ti atoms in the framework, giving rise to EI processes from the CS state of NR to the Ti trap states.

At a higher Ti doping the fs-behaviour becomes more like the one of the single doped Ti-MCM41 samples. The τ_1 component is due to the EI process to the Ti trap states. However, the time constants in these complexes are longer than those observed for TiMCM41-(3%) samples, which indicates that the Lewis acidity in these hosts has been affected by the presence of the Al atom and, as a result of the delocalization of the Brønsted acidity, the times of the ultrafast dynamics changes.

In summary, the coexistence of Ti and Al atoms in the MCM41 matrix modifies the ultrafast dynamics of interacting NR populations in comparison with the single-metal doped MCM41. These observations can be explained in terms of the electronegativity variations in the framework, as well as in terms of the possible modification of the Ti site geometry. [11, 37, 38] As a result, the specific and non-specific interactions NR/X-Y-MCM41 are affected, leading to an increment of the Brønsted acidity and simultaneous reduction of the Lewis acidity in comparison with the MCM41 doped only with Al or Ti, respectively. Scheme 1 summarizes the observed dynamics for double-metal doped MCM41 containing NR monomers, H-and J-aggregates.

4. Conclusion

In this work, we have reported on the photobehaviour (spectral and time domains) of NR interacting with simultaneously doped Ti- and Al-MCM41 mesoporous materials in DCM suspensions. Furthermore, the influence of the MCM41 framework composition (of different Si/X atomic ratios, X= Al, Ti) on the NR interactions with these materials at S_0 and S_1 were also investigated. The results show that upon interaction with MCM41 at different Si/Al ratios, the NR populations experience a small change when compared to the NR/R-MCM41 samples. This is due to a charge delocalization on the framework upon Al doping, which causes a small influence on its Brønsted acidity. On the other hand, the interactions with of NR with the Ti-MCM41 host are site-specific localized, for which the trap states population increases with the Ti doping. The presence of the trap states induces an ultrafast EI process from the photoproduced CS state to populate them.

For the co-metal-doped MCM41 materials (the Ti-Al-MCM41 ones), the interactions of NR with this material show a competition between Brønsted (Al doping) and Lewis (Ti doping) acid sites. Our results suggest that Al presence in the co-doped Al-Ti-MCM41 modifies the electronegativity, as well as changes the Ti coordination number and geometry in the framework, leading to a reduction of Lewis acidity.

The reported findings and the related discussion bring new knowledge for a better understanding the physicochemical properties of the metal-doped silica-based materials and the specific and non-specific interactions with an aromatic guest molecule. Moreover, the results and the acquired knowledge might be relevant to topics related to photocatalysis and photonics.

Acknowledgment: This work was supported by the MINECO and JCCM through Projects Consolider Ingenio 2010 (CDS2009-0050), PRI-PIBIN-2011-1283, MAT2011-25472, MAT2012-38567-C02-01, PROMETEOII/2013/011 and PEII-2014-003-P.

References

1. F. E. Kühn, Wiley Online Library, 2013.
2. D. Zhao, Y. Wan and W. Zhou, *Ordered Mesoporous Materials*, John Wiley & Sons, 2012.
3. C. Perego and R. Millini, Porous Materials in Catalysis: Challenges for Mesoporous Materials, *Chem. Soc. Rev.*, 2013, **42**, 3956-3976.
4. A. Corma, From Microporous to Mesoporous Molecular Sieve Materials and Their Use in Catalysis, *Chem. Rev.*, 1997, **97**, 2373-2420.
5. C. Yu and J. He, Synergic Catalytic Effects in Confined Spaces, *Chem. Commun.*, 2012, **48**, 4933-4940.
6. N. Pal and A. Bhaumik, Mesoporous Materials: Versatile Supports in Heterogeneous Catalysis for Liquid Phase Catalytic Transformations, *RSC Adv.*, 2015, **5**, 24363-24391.
7. M. J. Climent, A. Corma, S. Iborra and M. J. Sabater, Heterogeneous Catalysis for Tandem Reactions, *ACS Catal.*, 2014, **4**, 870-891.
8. R. Raja, M. E. Potter and S. H. Newland, Predictive Design of Engineered Multifunctional Solid Catalysts, *Chem. Commun.*, 2014, **50**, 5940-5957.
9. M. J. Climent, A. Corma and S. Iborra, Heterogeneous Catalysts for the One-Pot Synthesis of Chemicals and Fine Chemicals, *Chem. Rev.*, 2010, **111**, 1072-1133.
10. E. Gianotti, U. Diaz, A. Velty and A. Corma, Designing Bifunctional Acid-Base Mesoporous Hybrid Catalysts for Cascade Reactions, *Catal. Sci. Technol.*, 2013, **3**, 2677-2688.
11. M. Boronat, A. Corma, M. Renz and P. M. Viruela, Predicting the Activity of Single Isolated Lewis Acid Sites in Solid Catalysts, *Chem. Eur. J.*, 2006, **12**, 7067-7077.
12. M. Boronat, P. Concepcion, A. Corma, M. T. Navarro, M. Renz and S. Valencia, Reactivity in the Confined Spaces of Zeolites: The Interplay between Spectroscopy and Theory to Develop Structure-Activity Relationships for Catalysis, *Phys. Chem. Chem. Phys.*, 2009, **11**, 2876-2884.
13. K. B. Yoon, Electron- and Charge-Transfer Reactions within Zeolites, *Chem. Rev.*, 1993, **93**, 321-339.
14. S. Hashimoto, Zeolite Photochemistry: Impact of Zeolites on Photochemistry and Feedback from Photochemistry to Zeolite Science, *J. Photochem. Photobiol., C*, 2003, **4**, 19-49.
15. K. P. F. Janssen, G. De Cremer, R. K. Neely, A. V. Kubarev, J. Van Loon, J. A. Martens, D. E. De Vos, M. B. J. Roeffaers and J. Hofkens, Single Molecule Methods for the Study of Catalysis: From Enzymes to Heterogeneous Catalysts, *Chem. Soc. Rev.*, 2014, **43**, 990-1006.
16. I. L. C. Buurmans and B. M. Weckhuysen, Heterogeneities of Individual Catalyst Particles in Space and Time as Monitored by Spectroscopy, *Nat Chem*, 2012, **4**, 873-886.
17. J. C. Scaiano and H. García, Intrazeolite Photochemistry: Toward Supramolecular Control of Molecular Photochemistry, *Acc. Chem. Res.*, 1999, **32**, 783-793.
18. V. G. Machado, R. I. Stock and C. Reichardt, Pyridinium N-Phenolate Betaine Dyes, *Chem. Rev.*, 2014, **114**, 10429-10475.
19. J. Jose and K. Burgess, Benzophenoxazine-Based Fluorescent Dyes for Labeling Biomolecules, *Tetrahedron*, 2006, **62**, 11021-11037.
20. A. K. Dutta, K. Kamada and K. Ohta, Spectroscopic Studies of Nile Red in Organic Solvents and Polymers, *J. Photochem. Photobiol., A*, 1996, **93**, 57-64.
21. A. Cser, K. Nagy and L. Biczók, Fluorescence Lifetime of Nile Red as a Probe for the Hydrogen Bonding Strength with Its Microenvironment, *Chem. Phys. Lett.*, 2002, **360**, 473-478.

22. A. Kawski, B. Kukliński and P. Bojarski, Photophysical Properties and Thermochromic Shifts of Electronic Spectra of Nile Red in Selected Solvents. Excited States Dipole Moments, *Chem. Phys.*, 2009, **359**, 58-64.
23. C. Martín, P. Piatkowski, B. Cohen, M. Gil, M. T. Navarro, A. Corma and A. Douhal, Ultrafast Dynamics of Nile Red Interacting with Metal Doped Mesoporous Materials, *J. Phys. Chem. C*, 2015, **119**, 13283-13296.
24. J. A. Organero, L. Tormo and A. Douhal, Caging Ultrafast Proton Transfer and Twisting Motion of 1-Hydroxy-2-Acetonaphthone, *Chem. Phys. Lett.*, 2002, **363**, 409-414.
25. N. Alarcos, B. Cohen and A. Douhal, Photodynamics of a Proton-Transfer Dye in Solutions and Confined within NaX and NaY Zeolites, *J. Phys. Chem. C*, 2014, **118**, 19431-19443.
26. A. Tuel, Modification of Mesoporous Silicas by Incorporation of Heteroelements in the Framework, *Microporous Mesoporous Mater.*, 1999, **27**, 151-169.
27. L. C. de Souza, J. R. Pardauil, J. Zamian, G. da Rocha Filho and C. F. da Costa, Influence of the Incorporated Metal on Template Removal from MCM-41 Type Mesoporous Materials, *J. Therm. Anal. Calorim.*, 2011, **106**, 355-361.
28. H. Kosslick, G. Lischke, B. Parlitz, W. Storek and R. Fricke, Acidity and Active Sites of Al-Mcm-41, *Appl. Catal., A*, 1999, **184**, 49-60.
29. A. Corma and H. García, Lewis Acids: From Conventional Homogeneous to Green Homogeneous and Heterogeneous Catalysis, *Chem. Rev.*, 2003, **103**, 4307-4366.
30. A. Taguchi and F. Schüth, Ordered Mesoporous Materials in Catalysis, *Microporous Mesoporous Mater.*, 2005, **77**, 1-45.
31. M. Kasha, H. R. Rawls and M. Ashraf El-Bayoumi, in *Pure Appl. Chem.*, 1965, vol. 11, p. 371.
32. A. S. Davydov, The Theory of Molecular Excitons, *Soviet Physics Uspekhi*, 1964, **7**, 145.
33. A. Eisfeld and J. S. Briggs, The J- and H-Bands of Organic Dye Aggregates, *Chem. Phys.*, 2006, **324**, 376-384.
34. M. L. Occelli, S. Biz and A. Auroux, Effects of Isomorphous Substitution of Si with Ti and Zr in Mesoporous Silicates with the MCM-41 Structure, *Appl. Catal., A*, 1999, **183**, 231-239.
35. M. D. Alba, Z. Luan and J. Klinowski, Titanosilicate Mesoporous Molecular Sieve MCM-41: Synthesis and Characterization, *J. Phys. Chem.*, 1996, **100**, 2178-2182.
36. M. Moliner and A. Corma, Advances in the Synthesis of Titanosilicates: From the Medium Pore Ts-1 Zeolite to Highly-Accessible Ordered Materials, *Microporous Mesoporous Mater.*, 2014, **189**, 31-40.
37. A. Corma, M. A. Camblor, P. Esteve, A. Martinez and J. Perezpariente, Activity of Ti-Beta Catalyst for the Selective Oxidation of Alkenes and Alkanes, *J. Catal.*, 1994, **145**, 151-158.
38. A. Doménech, A. Corma, H. García and S. Valencia, Electrochemical Characterization of Two Different Framework Ti(Iv) Species in Ti/Beta Zeolites in Contact with Solvents, *Topics in Catalysis*, 2000, **11-12**, 401-407.
39. V. Ivády, I. A. Abrikosov, E. Janzén and A. Gali, Role of Screening in the Density Functional Applied to Transition-Metal Defects in Semiconductors, *Phys. Rev. B*, 2013, **87**, 205201.
40. F. Beeler, O. K. Andersen and M. Scheffler, Electronic and Magnetic Structure of 3d-Transition-Metal Point Defects in Silicon Calculated from First Principles, *Phys. Rev. B*, 1990, **41**, 1603-1624.
41. T. Blasco, A. Corma, M. T. Navarro and J. P. Pariente, Synthesis, Characterization, and Catalytic Activity of Ti-MCM-41 Structures, *J. Catal.*, 1995, **156**, 65-74.

42. L. Marchese, E. Gianotti, V. Dellarocca, T. Maschmeyer, F. Rey, S. Coluccia and J. M. Thomas, Structure-Functionality Relationships of Grafted Ti-MCM41 Silicas. Spectroscopic and Catalytic Studies, *Phys. Chem. Chem. Phys.*, 1999, **1**, 585-592.
43. A. Ya. Freidzon, A. A. Safonov, A. A. Bagaturyants and M. V. Alfimov, Solvatofluorochromism and Twisted Intramolecular Charge-Transfer State of the Nile Red Dye, *Int. J. Quantum Chem.*, 2012, **112**, 3059-3067.
44. C. Martin, B. Cohen, I. Gaamoussi, M. Ijjaali and A. Douhal, Ultrafast Dynamics of C30 in Solution and within CDs and HSA Protein, *J. Phys. Chem. B*, 2014, **118**, 5760-5771.
45. R. Jimenez, G. R. Fleming, P. V. Kumar and M. Maroncelli, Femtosecond Solvation Dynamics of Water, *Nature*, 1994, **369**, 471-473.

TOC: Spectroscopic and photodynamical characterizations of Nile Red interacting with Brønsted and Lewis acid sites within single- and multi-metal(X)-doped MCM41 materials (X= Ti and/or Al).

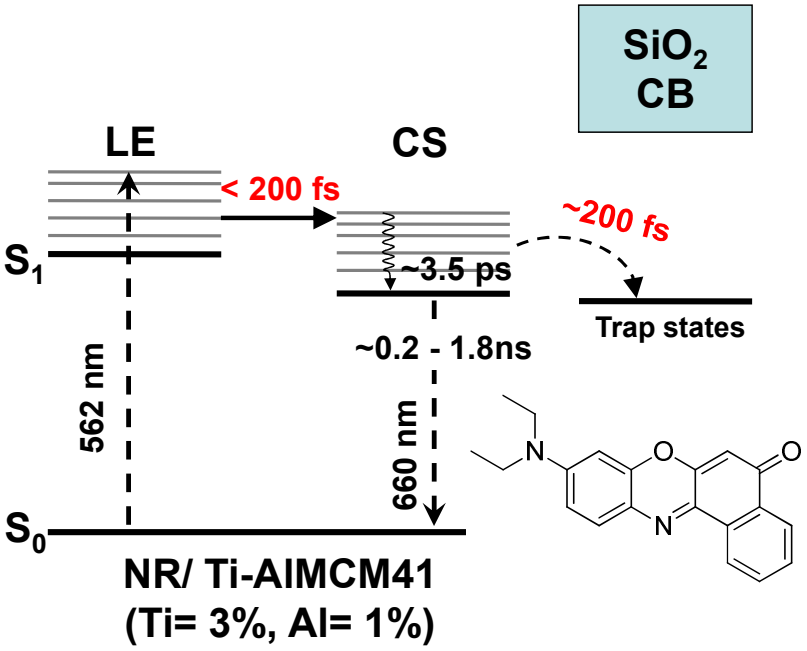

Table and Figure Captions

Scheme 1. A) Schematic presentation (not in scale) of the photodynamics of NR interacting with Ti-Al-MCM41 materials in DCM suspensions. B) Illustration of the NR populations within Al-Ti-MCM41 material.

Table 1. Values of the fluorescence lifetimes (τ_i) and normalized (to 100) pre-exponential factors (a_i) obtained from a global multiexponential fit of the emission decays of NR interacting with Ti-MCM41 (Ti doping= 1%, 3% and 5%) and Al-MCM41 (Al doping= 1% and 3%) in DCM suspensions upon excitation at 635 nm. The associated errors from the exponential decay fits are about ~ 10 - 15 %.

Table 2. Values of the fluorescence lifetimes (τ_i) and normalized (to 100) pre-exponential factors (a_i) obtained from a global multiexponential fits to the emission decays of NR at different concentrations interacting with Ti-Al-MCM41-(1%,1%) (Al and Ti doping ratios are 1% and 1%, respectively)and Ti-Al-MCM41-(3%,1%) (Al and Ti doping percent are 1% and 3%, respectively). The excitation and observation wavelengths were at 635 and 670 nm, respectively. The associated errors from the exponential decay fits are about ~ 10 - 15 %.

Table 3. Values of time constants (τ_i) and normalized (to 100) pre-exponential factors (A_i) of the multiexponential functions used to fit the fs-emission signals upon excitation at 562 nm of NR (DCM suspensions) interacting with: A) Al-MCM41 and Ti-MCM41 at different Si/X atomic ratio in DCM suspensions, and B) Ti-Al-MCM41-(1%,1%) and Ti-Al-MCM41-(3%,1%). Negative values of the amplitudes indicate rising components. The τ_3 time constant values were fixed in the fit using obtained in the ps-experiments. The associated errors from the exponential decay fits are about ~ 10 - 15 %.

Figure 1. Diffuse transmittance (DT) spectra (normalized to the maximum of intensity) of NR interacting with X-MCM41 in DCM suspensions: A) R-MCM41 and Al-MCM41 at different Al contents in the framework, B) R-MCM41 and Ti-MCM41 at different Ti contents in the matrix, and C) Ti-MCM41-(1%), Al-MCM41-(1%), Ti-Al-MCM41-(1%,1%) and Ti-Al-MCM41- (3%,1%), (Al content 1%).

Figure 2. Emission (normalized to the maximum of intensity) spectra of NR interacting with X-MCM41 in DCM suspensions, and upon excitation at 600 nm: A) R-MCM41 and Al-MCM41 at different Al contents in the framework, B) R-MCM41 and Ti-MCM41 at different

Ti contents in the matrix, and C) Ti-MCM41-(1%), Al-MCM41-(1%), Ti-Al-MCM41-(1%,1%) and Ti-Al-MCM41-(3%,1%).

Figure 3. Normalized (to the maximun of intensity) magic-angle emission decays of NR interacting with: A) R-MCM41, Al-MCM41-(1%) and Al-MCM41-(3%) , B) R-MCM41, Ti-MCM41-(1%), Ti-MCM41-(3%) and Ti-MCM41-(5%) and C) Ti-MCM41-(1%), Al-MCM41-(1%), Ti-Al-MCM41-(1%,1%) and Ti-Al-MCM41-(3%,1%) in DCM suspensions and upon excitation at 635 nm. The solid lines are from the best multiexponential fits to the experimental data. IRF is the instrumental response function (~80 ps). The observation wavelength was 670 nm.

Figure 4. Magic-angle femtosecond-emission transients of NR interacting with R-MCM41, Al-MCM41-(1%) and Al-MCM41-3% materials in DCM suspensions observed at A) 650 nm and B) 700 nm (λ_{ex} = 562 nm). The solid lines are from the best multiexponential fits of the experimental data, and the IRF is the instrumental response function (~200 fs).

Figure 5. Magic-angle femtosecond-emission transients of NR interacting with R-MCM41(black, solid squares), Ti-MCM41-(1%) (red, solid circles), Ti-MCM41-(3%) (blue, open squares) and Ti-MCM41-(5%) (green, solid triangles) materials observed at A) 650 nm and B) 700 nm (λ_{ex} = 562 nm). The solid lines are from the best multiexponential fits of the experimental data, and the IRF is the instrumental response function (~200 fs).

Figure 6. Comparison of the magic-angle femtosecond-emission transients of NR interacting with Ti-MCM41-(1%), Al-MCM41-(1%), Ti-Al-MCM41-(1%,1%) and Ti-Al-MCM41-(3%,1%) materials observed at A) 650 nm and B) 700 nm (λ_{ex} = 562 nm). The solid lines are from the best multiexponential fits of the experimental data, and the IRF is the instrumental response function (~200 fs).

Scheme 1

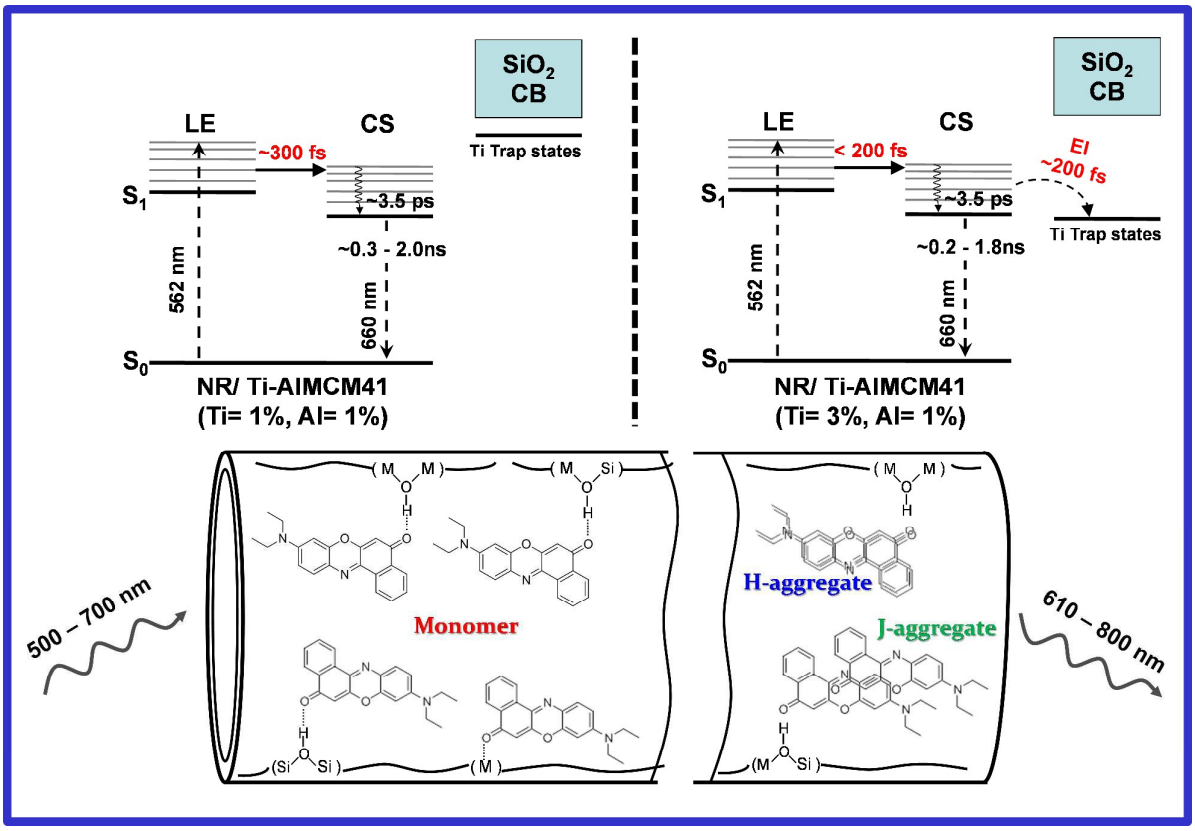

Table 1

Host	% M	λ_{em} / nm	τ_1 / ns	a_1 / %	τ_2 / ns	a_2 / %	τ_3 / ns	a_3 / %
Ti-MCM41	1	650	0.16	41	0.74	36	1.96	23
		670		45		35		19
		700		49		36		15
		730		49		37		14
		750		49		38		13
	3	650	0.09	60	0.55	26	1.82	14
		670		61		27		12
		700		63		28		9
		730		64		28		8
		750		65		27		8
	5	650	0.07	66	0.40	23	1.47	11
		670		67		24		9
		700		69		24		7
		730		68		25		7
		750		69		24		6
Al-MCM41	1	650	0.34	27	1.28	59	2.7	14
		670		24		62		14
		700		25		63		12
		730		27		62		11
		750		26		63		11
	3	650	0.31	29	1.17	53	2.7	18
		670		21		62		17
		700		18		67		15
		730		23		63		14
		750		21		67		12

Table 2

Host	% Ti	% Al	λ_{em} / nm	τ_1 / ns	a_1 / %	τ_2 / ns	a_2 / %	τ_3 / ns	a_3 / %
Ti-Al-MCM41	1	1	650	0.29	29	0.94	39	2.00	32
			670		24		46		30
			700		25		48		27
			730		26		48		26
			750		26		49		25
	3	1	650	0.20	31	0.74	40	1.80	28
			670		31		44		25
			700		32		46		22
			730		33		46		21
			750		34		46		20

Table 3
A

λ_{em}/nm	τ_i	Ti-MCM41			Al-MCM41	
		1%	3%	5%	1%	3%
		τ_i (A_i %)				
630	τ_1 / ps	0.22 (54)	0.17 (51)	0.14 (51)	0.37 (29)	0.35 (36)
	τ_2 / ps	2.22 (19)	1.81 (23)	1.69 (25)	3.20 (9)	3.23 (18)
	τ_3^* / ns	0.16 (27)	0.09 (26)	0.07 (24)	0.30 (62)	0.30 (46)
650	τ_1 / ps	0.28 (25)	0.17 (46)	0.15 (48)	0.32 (13)	0.33 (12)
	τ_2 / ps	2.41 (22)	1.75 (20)	1.70 (25)	3.35 (7)	4.02 (10)
	τ_3^* / ns	0.16 (53)	0.09 (34)	0.07 (27)	0.30 (80)	0.30 (78)
670	τ_1 / ps	0.28 (13)	0.16 (32)	0.15 (30)	0.31 (-100)	0.30 (-100)
	τ_2 / ps	2.54 (19)	1.87 (26)	1.75 (29)	-	-
	τ_3^* / ns	0.16 (68)	0.09 (42)	0.07 (41)	0.30 (100)	0.30 (94)
700	τ_1 / ps	-	-	-	0.32 (-100)	0.30 (-100)
	τ_2 / ps	2.33 (25)	1.77 (39)	1.71 (55)	-	-
	τ_3^* / ns	0.16 (75)	0.09 (61)	0.07 (45)	0.30 (100)	0.30 (100)

B

λ_{em}/nm	τ_i	1% (Ti) 1% (Al)	3% (Ti) 1% (Al)
		τ_i (A_i %)	
630	τ_1 / ps	0.30 (26)	0.21 (28)
	τ_2 / ps	2.42 (16)	1.85 (18)
	τ_3^* / ns	0.30 (58)	0.20 (54)
650	τ_1 / ps	0.29 (10)	0.20 (5)
	τ_2 / ps	2.51 (10)	1.91 (16)
	τ_3^* / ns	0.30 (80)	0.20 (79)
670	τ_1 / ps	0.28 (-100)	-
	τ_2 / ps		1.88 (14)
	τ_3^* / ns	0.30 (97)	0.20 (86)
700	τ_1 / ps	0.28 (-100)	-
	τ_2 / ps		1.90 (15)
	τ_3^* / ns	0.30 (99)	0.20 (85)

Figure 1

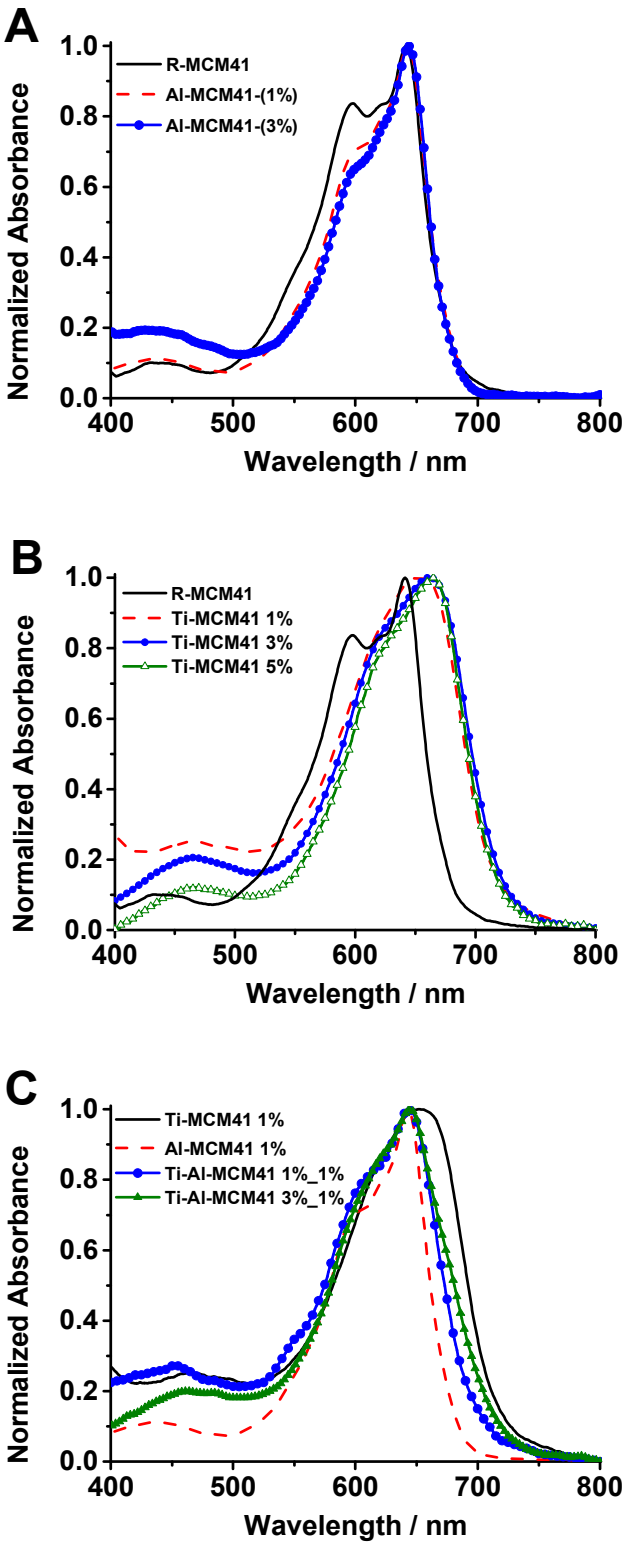

Figure 2

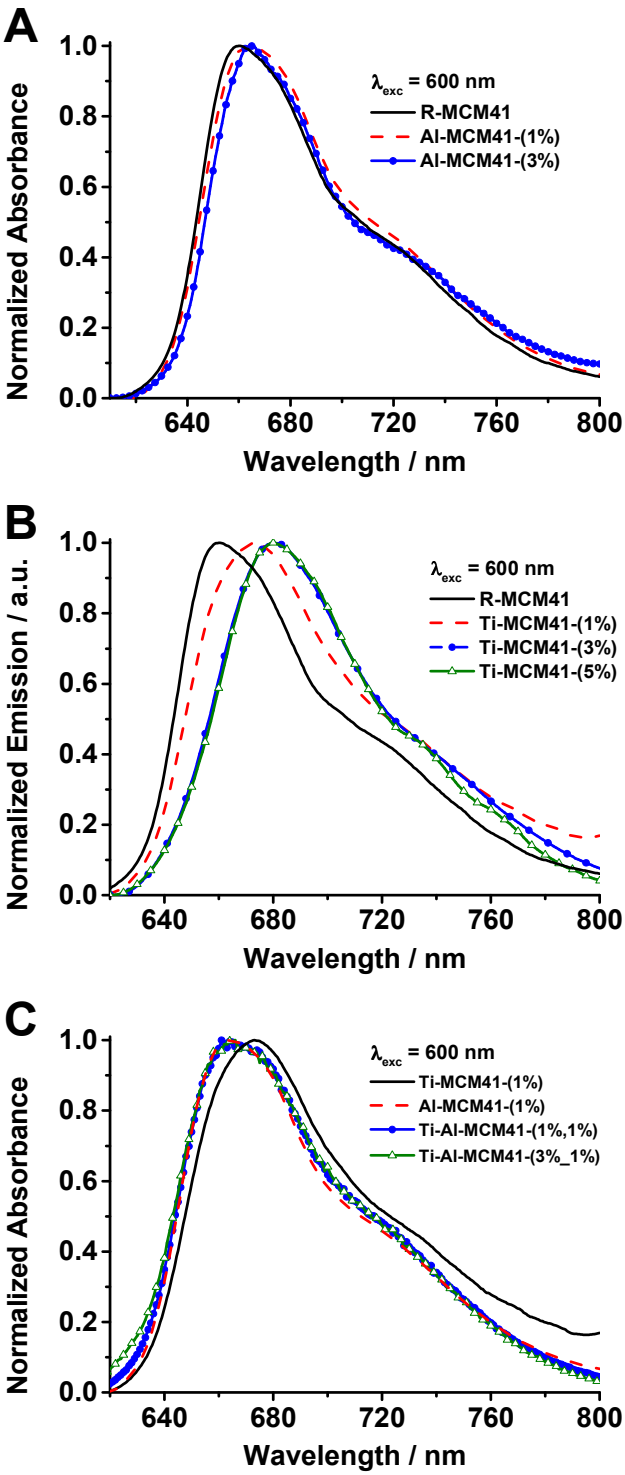

Figure 3

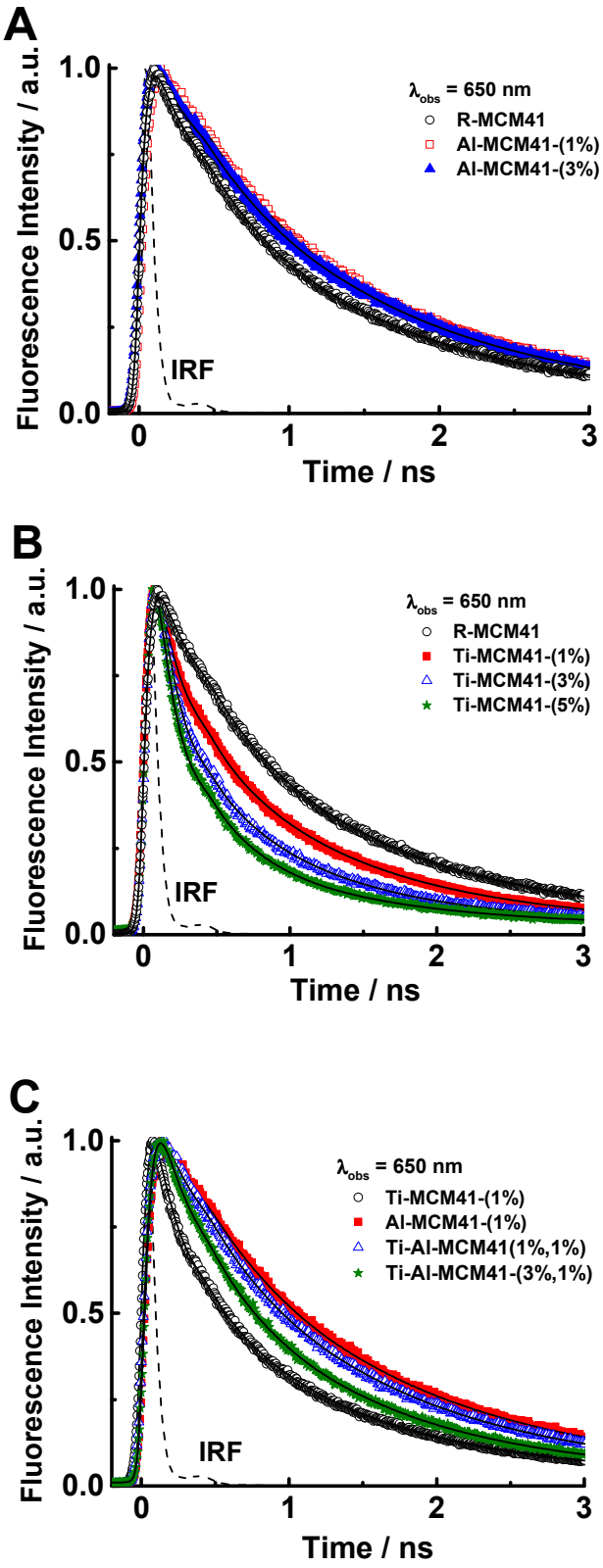

Figure 4

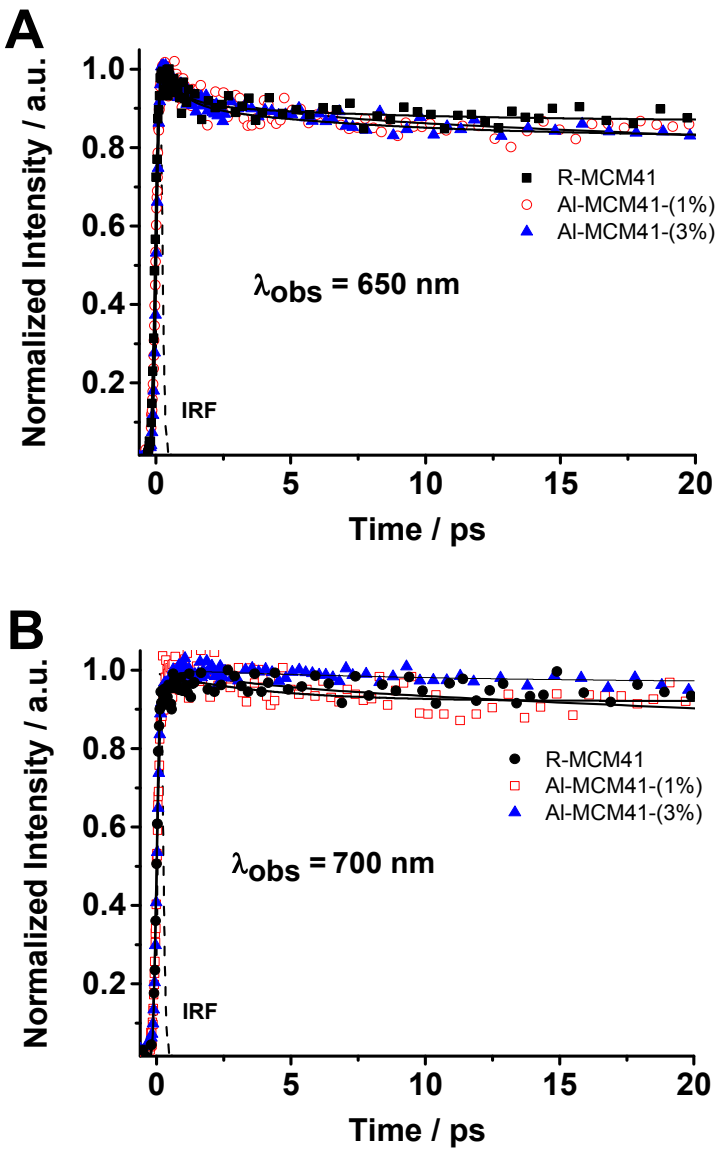

Figure 5

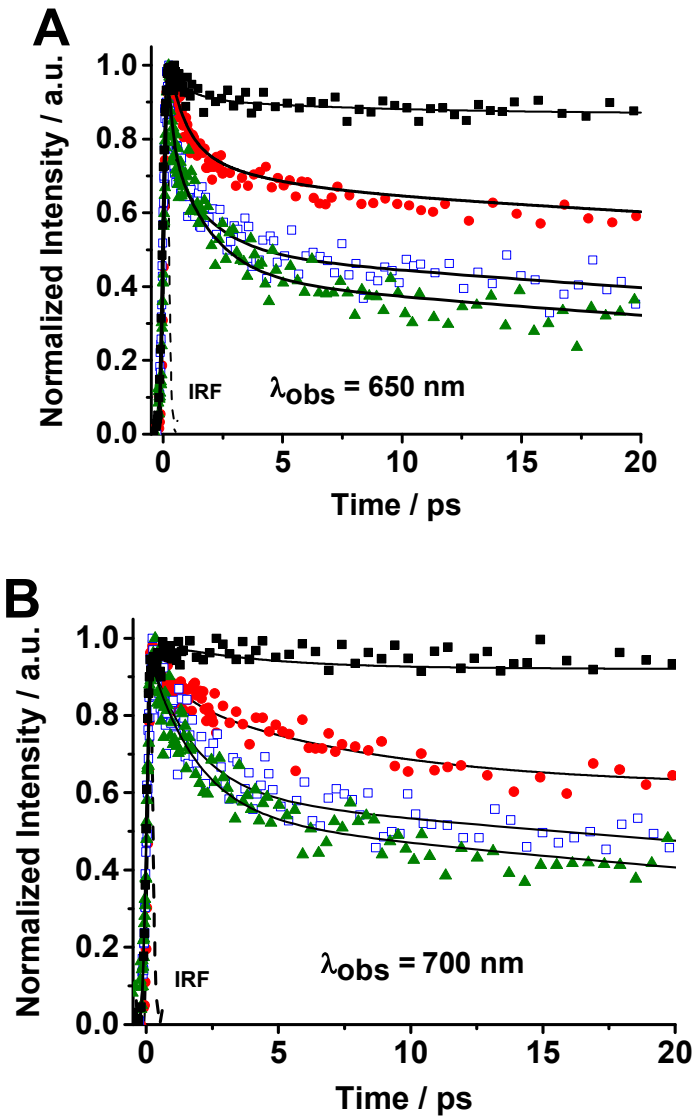

Figure 6